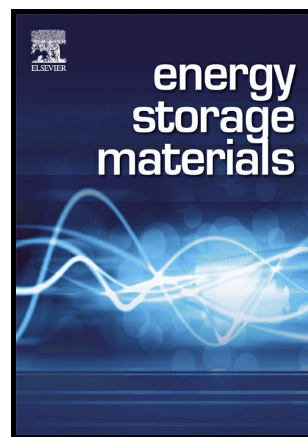# Author's Accepted Manuscript

Growth and growth mechanism of oxide nanocrystals on electrochemically exfoliated graphene for lithium storage

Zexuan Xu, Ping Zhang, Jialu Chen, Wenbo Yue, Wuzong Zhou

energy
storage
materials

www.elsevier.com/locate/ensm

Cite this article as: Zexuan Xu, Ping Zhang, Jialu Chen, Wenbo Yue and Wuzong Zhou, Growth and growth mechanism of oxide nanocrystals on electrochemically exfoliated graphene for lithium storage, *Energy Storage Materials,* https://doi.org/10.1016/j.ensm.2018.08.023

Growth and growth mechanism of oxide nanocrystals on electrochemically exfoliated graphene for lithium storage

Zexuan Xu,[a] Ping Zhang,[a] Jialu Chen,[b] Wenbo Yue,[a,*] Wuzong Zhou [b,*]

[a] Beijing Key Laboratory of Energy Conversion and Storage Materials, College of Chemistry, Beijing Normal University, Beijing, 100875, China.

[b] School of Chemistry, University of St Andrews, St Andrews, Fife KY16 9ST, UK.

E-mail address: wbyue@bnu.edu.cn (W.B. Yue).

E-mail: wzhou@st-andrews.ac.uk (W.Z. Zhou)

[*]Corresponding authors. Tel.: +86 10 58804229; Fax: +86 10 58802075.

Abstract

Difficulty of growing metal oxides on intrinsic graphene due to few defects and functional groups on its surface was overcome by deposition of polymerized precursors via multiple interacting sites, followed by crystallization of metal oxides inside the aggregated polymer. As a typical example, Mn_3O_4-decorated electrochemically exfoliated graphene (EEG) was successfully prepared and served as an advanced anode material for lithium-ion batteries. Because EEG possesses higher electronic conductivity and stronger mechanical strength in comparison with commonly used reduced graphene oxide (rGO), the new composite of EEG-Mn_3O_4 exhibits much better electrochemical performance than rGO-Mn_3O_4, including superior reversible capacity and better cycling stability.

1

Graphical abstract:

Keywords:

electrochemically exfoliated graphene; trimanganese tetraoxide; polymerization; gentle

synthesis; lithium-ion batteries

1. Introduction

As a novel two dimensional carbon nanomaterial, graphene has attracted wide attention due to its unique properties such as large surface area, outstanding mechanical strength, and high electrical and thermal conductivities [1,2]. As an important application, graphene has been used as an ideal substrate to support various functional materials, in order to improve their properties for a variety of applications [3-5]. A case in point is graphene-Mn_3O_4 composite used as an electrode material for lithium-ion batteries (LIBs), supercapacitors and fuel cells [6-8].

Mn_3O_4 has many advantages in this field such as high theoretical capacities (~936 mA h g^{-1}), high abundance and low cost [9,10]. However, some drawbacks such as severe volume change during cycling, and poor electrical conductivity (~10^{-7}−10^{-8} S cm^{-1}) hamper its practical applications [6].

2

Integration of Mn_3O_4 with graphene can enhance the electrical conductivity, and restrain the volume variation of Mn_3O_4 particles to some extent due to the interaction of Mn_3O_4 with graphene. However, growing metal oxide nanocrystals on intrinsic graphene is extremely difficult, because the inert surface of graphene hardly adsorb precursor molecules/ions for crystal growth. In practice, to make graphene as suitable substrates for crystal growth, the graphene is often oxidised into graphene oxide (GO), that possesses many oxygen-containing functional groups on the surface (e.g., carboxyl, hydroxyl, carbonyl and epoxide groups) [11,12]. To restore partly the lost electrical conductivity, reduced graphene oxide (rGO) is normally obtained by thermal or chemical reduction of GO. However, even after the reduction, many defects are still residual on the surface of rGO, leading to a dramatic decrease of its electrical conductivity and mechanical strength in comparison with intrinsic graphene.

Recently, graphene with few O-containing groups has been mass-produced, such as electrochemically exfoliated graphene (EEG) [13,14]. Like intrinsic graphene fabricated by other exfoliation methods [15], the EEG contains few defects and, therefore, has a higher electrical conductivity (235.9 S cm^{-1}) (**Table 1**) and stronger mechanical strength than rGO. It is expected that EEG-Mn_3O_4 would display better electrochemical performance as a LIB anode material than rGO-Mn_3O_4. However, it was found that metal oxide crystals tend to grow and anchor at O-containing defect sites of GO [16,17], and therefore, the inert surface of EEG would not be a suitable base for growing crystals. In addition, unlike hydrophilic GO, the hydrophobic EEG tends to aggregate in water via π−π interactions (**Fig. S1**) [18-21]. Thus using a polar aprotic solvent, such as N,N-dimethylformamide (DMF), has to be considered in the solution synthesis of EEG-Mn_3O_4 [13].

Table 1. The electrical conductivity (C), intensity ratios of Raman D band and G band (I_D/I_G), SEI film resistances (R_f) and charge-transfer resistances (R_{ct}) of EEG, GO, EEG-Mn_3O_4, rGO-Mn_3O_4 and HrGO-Mn_3O_4.

Sample	C / S cm^{-1}	I_D/I_G	R_f / Ω	R_{ct} / Ω
EEG	235.9	0.29	N/A	N/A
GO	6.2×10^{-6}	1.13	N/A	N/A
EEG-Mn_3O_4	24.0	0.33	17.0	32.6
rGO-Mn_3O_4	6.1	1.11	24.7	143.3
HrGO-Mn_3O_4	14.5	1.10	17.2	61.8

Consequently, EEG is much less popular than rGO in fabrication of graphene-nanocrystal composites. Wei, et al. tried to assemble EEG nanosheets with a series of functional nanoparticles by using polyaniline as a versatile dopant [22]. However, such a complicated noncovalent linkage is unfavorable to the enhancement of electron transfer and chemical stability of the EEG hybrids [17]. Direct growth of functional materials on EEG is still a big challenge.

Herein we demonstrate a successful growth of Mn_3O_4 nanocrystals on EEG in DMF under gentle conditions (water bath at 80 °C for 1 h), by using a polymerizable precursor, Mn(II) acetylacetonate, Mn(acac)$_2$. The new composite of EEG-Mn_3O_4 exhibits excellent electrochemical performance, including superior reversible capacity (909 mA h g^{-1}) and better cycling stability. The new growing mechanism of Mn_3O_4 nanocrystals on EEG was investigated in detail. rGO-Mn_3O_4 was also prepared under the same conditions, and showed a worse electrochemical performance in comparison

with EEG-Mn_3O_4. It should be noted that although Mn_3O_4 has some practical issues as an anode material for LIBs, the research in this work focuses on the advantages of EEG in hybrids, which acts as a promising graphene substrate instead of rGO. Thus this novel strategy for the synthesis of EEG-supported metal oxides provides access to a wide range of EEG hybrids with high performance, which could be applied in various fields such as batteries and fuel cells.

2. Experimental section

2.1 Sample preparation

EEG and GO. EEG was synthesised according to the published literature (**Fig. S2**) [13]. Natural graphite flakes were used as an anode and Pt wire was used as a cathode for electrochemical exfoliation of graphite. The electrolyte solution was prepared by dissolving 1.32 g of $(NH_3)_2SO_4$ in 100 mL of distilled water (0.1 M). The distance between the graphite and the Pt electrode was ~2 cm. Electrochemical exfoliation was carried out by applying positive voltage to the graphite electrode. The electrolytic voltage was kept at 5 V for 10 min, and then increased to 10 V for another 10 min. After the exfoliation, the product was collected through a polytetrafluoroethylene (PTFE) membrane filter with 0.25 μm pore size and washed several times with distilled water by vacuum filtration. After drying in oven, the product was dispersed in N,N-dimethylformamide (DMF) by sonication for 1 h. The suspension was then maintained for 12 h. The top part of suspension was collected for late use.

GO was synthesised from natural graphite powders by a modified Hummers' method [23]. In a typical synthesis, 5 g of graphite powder and 5 g of $NaNO_3$ were added into 230 mL of 98% H_2SO_4 under stirring in an ice bath. 30 g of $KMnO_4$ was slowly added

to the suspension under stirring for 15 min below 5 °C. The suspension was then heated at 35 °C for 30 min. Subsequently, 460 mL of distilled water was slowly added into the above suspension, followed by stirring at 98 °C for more than 15 min. The suspension was further diluted with 1400 mL of distilled water and the reaction was terminated by adding 25 mL of 30 % H_2O_2. Meanwhile, the colour of the solution turned from dark brown to bright yellow. The resulting GO nanosheets were filtered and washed with distilled water several times to remove residual acids and salts. As-prepared GO was dispersed in water by ultrasonication for 30 min, followed by a low-speed centrifugation to get rid of any aggregated GO nanosheets.

EEG-Mn$_3$O$_4$ and rGO-Mn$_3$O$_4$. In a typical synthesis, 0.02 g of EEG (or GO) was dispersed in 100 mL of DMF solution by sonication for 1 h. 0.20 g of Mn(acac)$_2$ and 10 mL of distilled water were then added into the above suspension with vigorous stirring for 30 min. This suspension was transferred into a round-bottomed flask and heated in a water bath at 80 °C for 1 h. The GO was partially reduced to rGO during this process, whereas EEG did not change much. After cooling down to room temperature, EEG-Mn$_3$O$_4$ (or rGO-Mn$_3$O$_4$) was collected by centrifugation, washed with distilled water, and dried at 60 °C. The Mn$_3$O$_4$ loading for the sample is expected to be about 60 wt%. For a low or high loading specimen, the amount of Mn(acac)$_2$ was simply reduced to 0.08 g or increased to 0.30 g. EEG-Mn$_3$O$_4$ was also prepared by using manganese acetate as the precursor. 0.23 g of Mn(Ac)$_2$·4H$_2$O was used instead of Mn(acac)$_2$, and the mixture solution was treated under solvothermal conditions at 180 °C for 12 h instead of in water bath.

HrGO-Mn$_3$O$_4$. rGO-Mn$_3$O$_4$ was dispersed in 70 mL of water by sonication for 1 h. This suspension was transferred into a 100 mL Teflon-lined stainless steel autoclave

6

and maintained at 180 °C for 10 h. The product, HrGO-Mn$_3$O$_4$, was collected by centrifugation, washed with distilled water, and dried at 60 °C.

2.2 Sample characterisation

Specimens were characterised by using the following techniques. X-ray diffraction (XRD) was performed on a Phillips X'pert Pro MPD diffractometer with Cu Kα radiation. The Fourier transform infrared (FT-IR) spectrometry was performed on a Nicolet-380 Fourier-transform infrared spectrometer in the range of 400-4000 cm^{-1}. X-ray photoelectron (XPS), was carried out on a Shimadzu Axis Ultra spectrometer with an Mg K$_α$ (1253.6 eV) excitation source, Raman scattering spectra were recorded on a Jobin-Yvon Laser Confocal Micro-Raman Spectrometer with a 633 nm laser source. Mass spectra were obtained on an AB Sciex TripleTOF 5600™ mass spectrometer. The thermogravimetric analysis (TGA) was carried out on a NETZSCH STA 409 PC/PG thermal analyser and carried out in air at a heating rate of 5 °C min^{-1}. Scanning electron microscopic (SEM) images were obtained on a JEOL JSM-6700F electron microscope at an accelerating voltage of 5 kV. Transmission electron microscopy (TEM) and high-resolution TEM (HRTEM) images and energy-dispersive X-ray (EDX) spectra were recorded on a FEI Titan Themis electron microscope operated at 200 kV.

2.3 Electrochemical measurement

For electrochemical characterisation, the composite electrodes were fabricated by mixing the active materials, Super P carbon black and polyvinylidenedifluoride (PVDF) dissolved in N-methyl-2-pyrrolidine (NMP) in a weight ratio of 80:10:10. The mixed slurry was pressed onto a copper foil and dried at 110 °C in vacuum for 24 h. Cell

assembly was carried out in an Ar-filled glove box. The electrolyte was 1 M solution of $LiPF_6$ dissolved in a EC:DEC:DMC solution with a 1:1:1 vol ratio. The area of the electrode was 2.0 cm^2 and the mass loading of active materials was about 2.5 mg cm^{-2}. Electrochemical performances were measured using a LR2032-type coin cell with lithium metal as the negative electrode. The galvanostatic charge–discharge performance was measured with a LAND test system at room temperature, and the voltage range was from 0.01 to 3.0 V (versus Li/Li^+), with a constant current of 0.1–2 C (1 C equals to 936 mA g^{-1} for Mn_3O_4-containing samples). Cyclic voltammetry tests were performed between 0.01 and 3.0 V with a scan rate of 0.5 mV s^{-1}, and the electrochemical impedance spectroscopy (EIS) was carried out in the frequency range from 100 kHz to 10 mHz on a Gamry Interface 1000 electrochemical station. The electrical conductivity of samples were measured by a four point probe set up from a Keithley 2400 source meter.

3. Results and discussion

3.1 Microstructures of the composites

Fig. 1 shows TEM and HRTEM images of a typical EEG-Mn_3O_4 nanosheet (~30 wt% loading), revealing that Mn_3O_4 nanocrystals with diameters of 12 to 16 nm are well-dispersed on the surface of EEG. The even dispersion is similar to that in rGO-Mn_3O_4 with a similar loading level (**Fig. 2**). TGA shows that the actual loadings of Mn_3O_4 are 32.1 wt% in EEG-Mn_3O_4 and 29.9 wt% in rGO-Mn_3O_4 (**Fig. S3a**). EDX spectrum of EEG-Mn_3O_4 shows three elements, C, O and Mn (**Fig. S4**).

The measured d-spacings from the nanocrystals on the HRTEM image of **Fig. 1c** confirm the tetragonal Mn_3O_4 structure. For example, the fringes with $d_A = 0.199$ nm,

d_C = 0.287 nm, and d_D = 0.303 nm can be indexed to (220), ($\bar{2}$00), and (112) planes of Mn$_3$O$_4$. A SAED pattern from a large area (inset of **Fig. 1c**) shows a set of diffraction rings, indicating randomly orientated Mn$_3$O$_4$ nanocrystals. The d-spacings calculated from these rings correspond to the planes in Mn$_3$O$_4$, d_A = 0.306 nm (112), d_B = 0.274 nm (103), d_C = 0.248 nm (211), d_D = 0.236 nm (004), d_E = 0.179 nm (105), d_F = 0.154 nm (224), d_G = 0.145 nm (400).

More importantly, the characteristic hexagonal lattice of graphene is also visible in the HRTEM image, indicative of the pristine regions of EEG with few defects. The d-spacing of ~0.21 nm (marked B in **Fig. 1c**) is assigned to (100) of graphite [24]. The corresponding SAED pattern from EEG is hexagonal as shown in the inset of **Fig. 1c**, where the marked spots H and I with d-spacings of 0.211 and 0.121 nm can be indexed to the (100) and (110) of the graphene structure. Another interesting feature of the HRTEM image in **Fig. 1c** is that the fringes 'A' of Mn$_3$O$_4$ are parallel and almost match the fringes 'B' of graphene, implying that a chemical interaction takes place between the nanocrystal and the EEG, although uniform orientation of nanocrystals on the same graphene sheet was not observed.
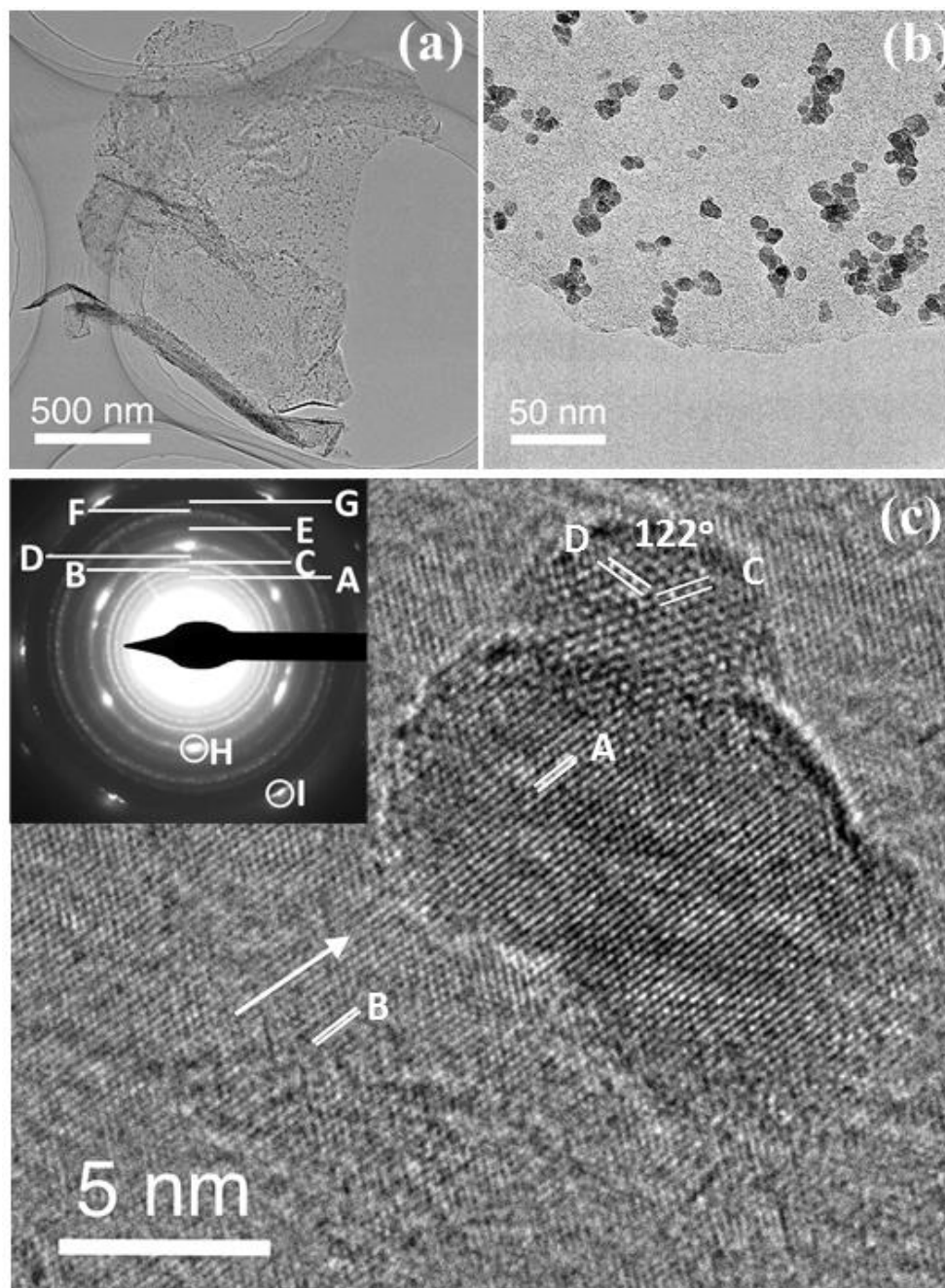
Fig. 1 (a) TEM image of an EEG nanosheet loaded ~30 wt% Mn_3O_4. (b) Enlarged TEM image. (c) HRTEM image of an area in (b). The inset is a SAED pattern from a large area.

On the contrary, the HRTEM image of rGO-Mn_3O_4 (**Fig. 2c**) shows much poor crystallinity of graphene with many residual defects after removal of O-containing

groups [25]. Nevertheless, the HRTEM images of Mn_3O_4 crystals and the SAED patterns of rGO-Mn_3O_4 are very similar to that of EEG-Mn_3O_4. The fringes with measured d-spacings $d_A = d_B = 0.490$ nm can be indexed to the (101) and (10$\bar{1}$) planes of Mn_3O_4, respectively. In the SAED pattern, the diffraction rings are from randomly oriented Mn_3O_4 nanocrystals, $d_A = 0.307$ nm (112), $d_B = 0.274$ nm (103), $d_C = 0.253$ nm (211), $d_D = 0.235$ nm (004), $d_E = 0.177$ nm (105), $d_F = 0.153$ nm (224), $d_G = 0.145$ nm (400). The diffraction spots forming a hexagonal pattern are from rGO, $d_H = 0.211$ nm (100) and $d_I = 0.121$ nm (110).

When a higher loading of Mn_3O_4 (~60 wt%) was applied in EEG-Mn_3O_4, the nanocrystals are more evenly distributed on EEG than on rGO (**Fig. 3**), although the average loading of Mn_3O_4 (58.6 wt%) is also close to that in rGO-Mn_3O_4 (56.8 wt%) (**Fig. S3b**). The surface functional groups of GO provide preferred nucleation sites for the growth of Mn_3O_4 nanocrystals, leading to the particle aggregation around the functional groups of GO [26-28]. Unlike GO, the EEG surface has much less oxygen-containing functional groups or defects. The deposition of oxide nanocrystallites on EEG replies on inter-molecular interactions. Therefore, the large contact area of EEG with polymerised precursors ensures a homogeneous distribution of Mn_3O_4 nanocrystals on EEG (the crystal growth mechanism will be discussed later). Since the electrochemical performance of both EEG-Mn_3O_4 and rGO-Mn_3O_4 was improved with the increase of the oxide loading (discussed below), our further investigation of these materials focused on the high loading specimens without further noting.
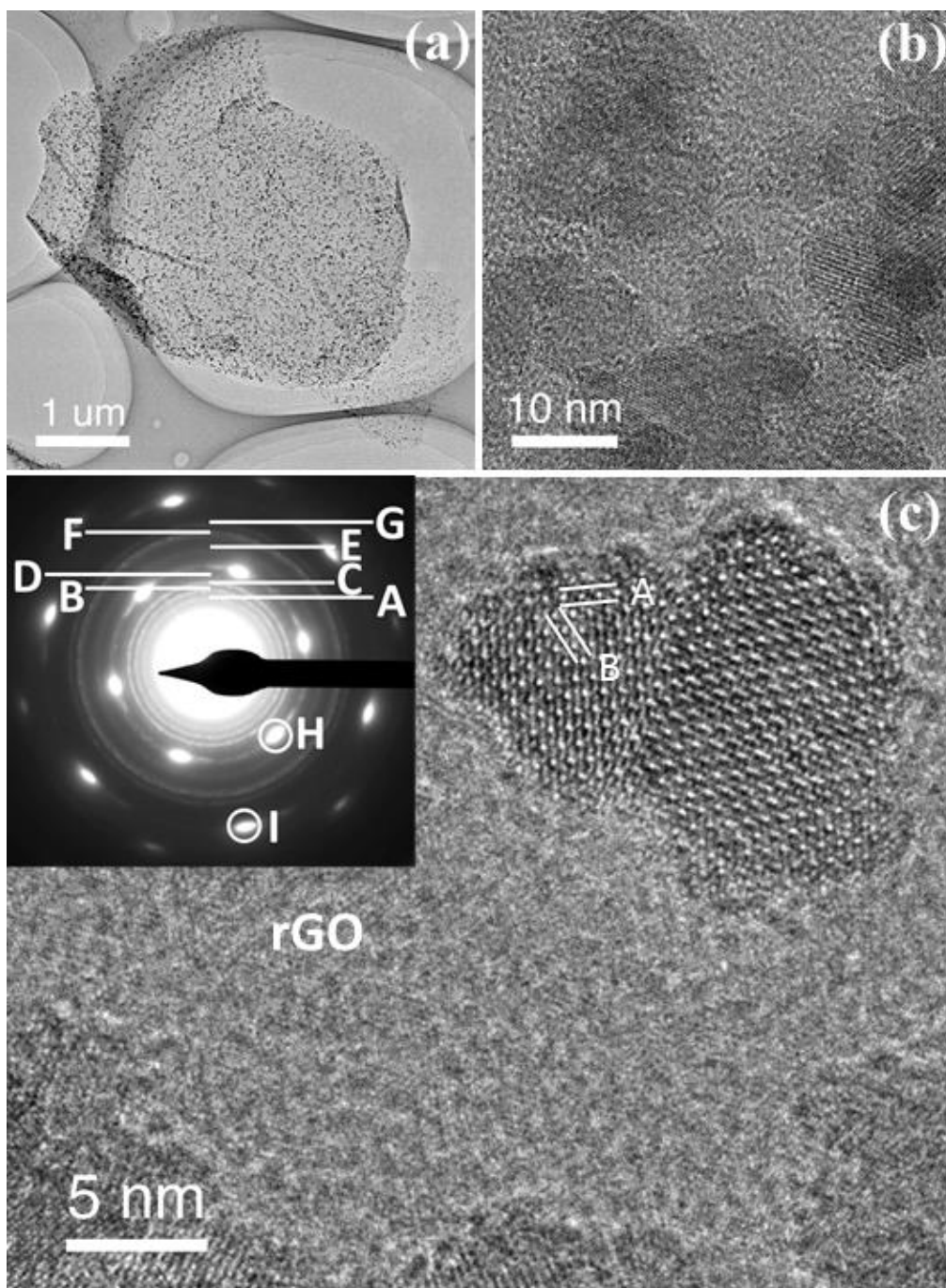
Fig. 2 (a) TEM image of a rGO nanosheet loaded ~30 wt% Mn_3O_4. (b) Corresponding HRTEM image. (c) Enlarged HRTEM image showing lattice fringes of both Mn_3O_4 nanocrystal and the rGO nanosheet. The inset is an SAED pattern from a large area.
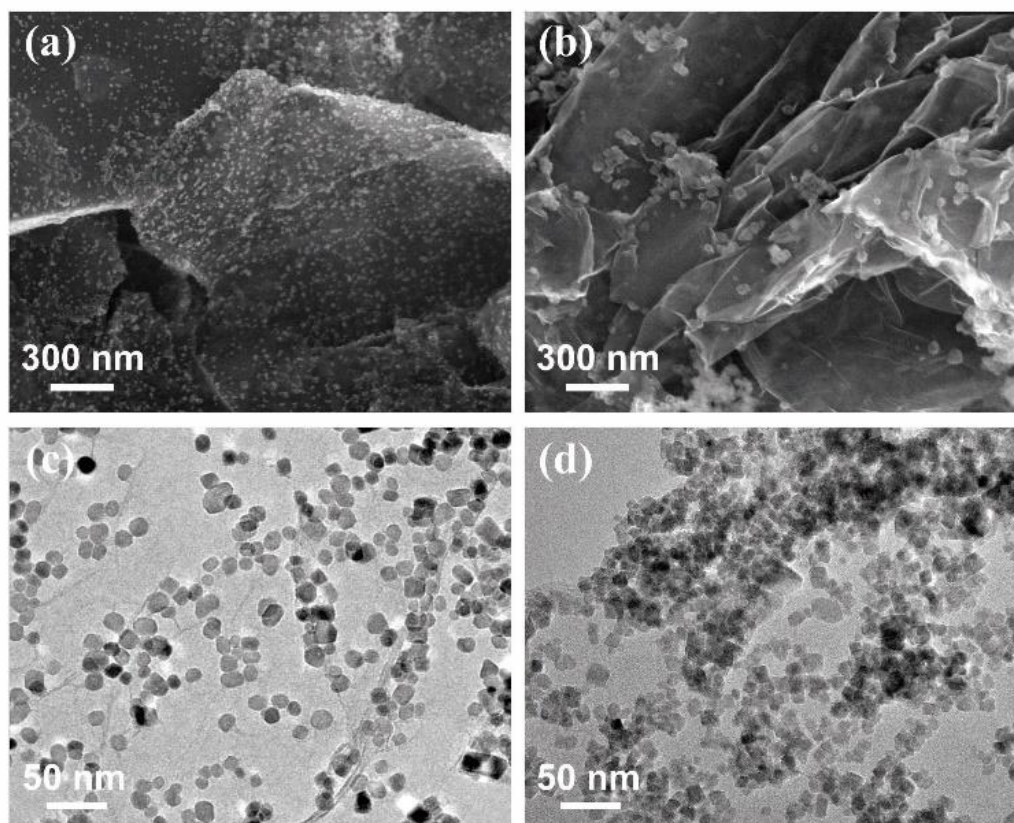
Fig. 3 SEM images of (a) EEG-Mn_3O_4 and (b) rGO-Mn_3O_4. TEM images of (c) EEG-Mn_3O_4 and (d) rGO-Mn_3O_4. The Mn_3O_4 loading on EEG or rGO nanosheet is ~60 wt%.

Both XRD patterns of EEG-Mn_3O_4 and rGO-Mn_3O_4 (**Fig. 4a**) show the diffraction peaks corresponding to the tetragonal Mn_3O_4. It is noted that the crystallinity of Mn_3O_4 on EEG is higher than that on rGO. The peak marked by an asterisk in the pattern of EEG-Mn_3O_4 is from graphene, which is too weak to be observed from rGO-Mn_3O_4.

XPS survey spectra of EEG-Mn_3O_4 and rGO-Mn_3O_4 show only three elements, C, O, and Mn (**Fig. 4b**). The intensity ratio of the C 1s to O 1s peaks from EEG-Mn_3O_4 is much higher than that from rGO-Mn_3O_4, implying that a significant number of O-containing functional groups in GO still remain in rGO. The C 1s peak in the high-resolution XPS spectrum of GO (**Fig. 4c**) can be divided into four components, which

13

are assigned to C–C (~284.6 eV), C–O (~286.6 eV), C=O (~287.6 eV) and O–C=O (~288.8 eV) groups, respectively [29,30]. In contrast, there is only one distinct peak corresponding to C–C group from EEG, demonstrating that EEG contains few O-containing functional groups. After water bath treatment, the peaks related to O-containing groups were still observed in the spectrum of rGO-Mn_3O_4 (**Fig. 4d**) though their intensities markedly decreased, while there is not much difference between the peaks in the spectra of EEG and EEG-Mn_3O_4. Apparently, GO cannot be completely reduced under this gentle synthesis condition (80 °C water bath), which may highly influence its electrical conductivity. On the other hand, it does not need to reduce EEG, since it has few O-containing groups in its initial state.

Raman spectra of GO and EEG (**Fig. 4e**) further confirm their notable structural difference. The D and G bands are related to the vibrations of nonplanar sp^3 and the in-plane sp^2 carbon atoms, respectively [31,32]. The intensity ratio of these bands (I_D/I_G) of GO is 1.13, much higher than that of EEG (0.29). It is obvious that GO possesses more defects than EEG. The I_D/I_G value of rGO-Mn_3O_4 (1.11), after the heat treatment, is close to that of GO, implying that many defects remain in rGO, even many O-containing groups having been eliminated from the surface (**Fig. 4f**). Mn_3O_4 loading on EEG does not change the I_D/I_G value much as well.
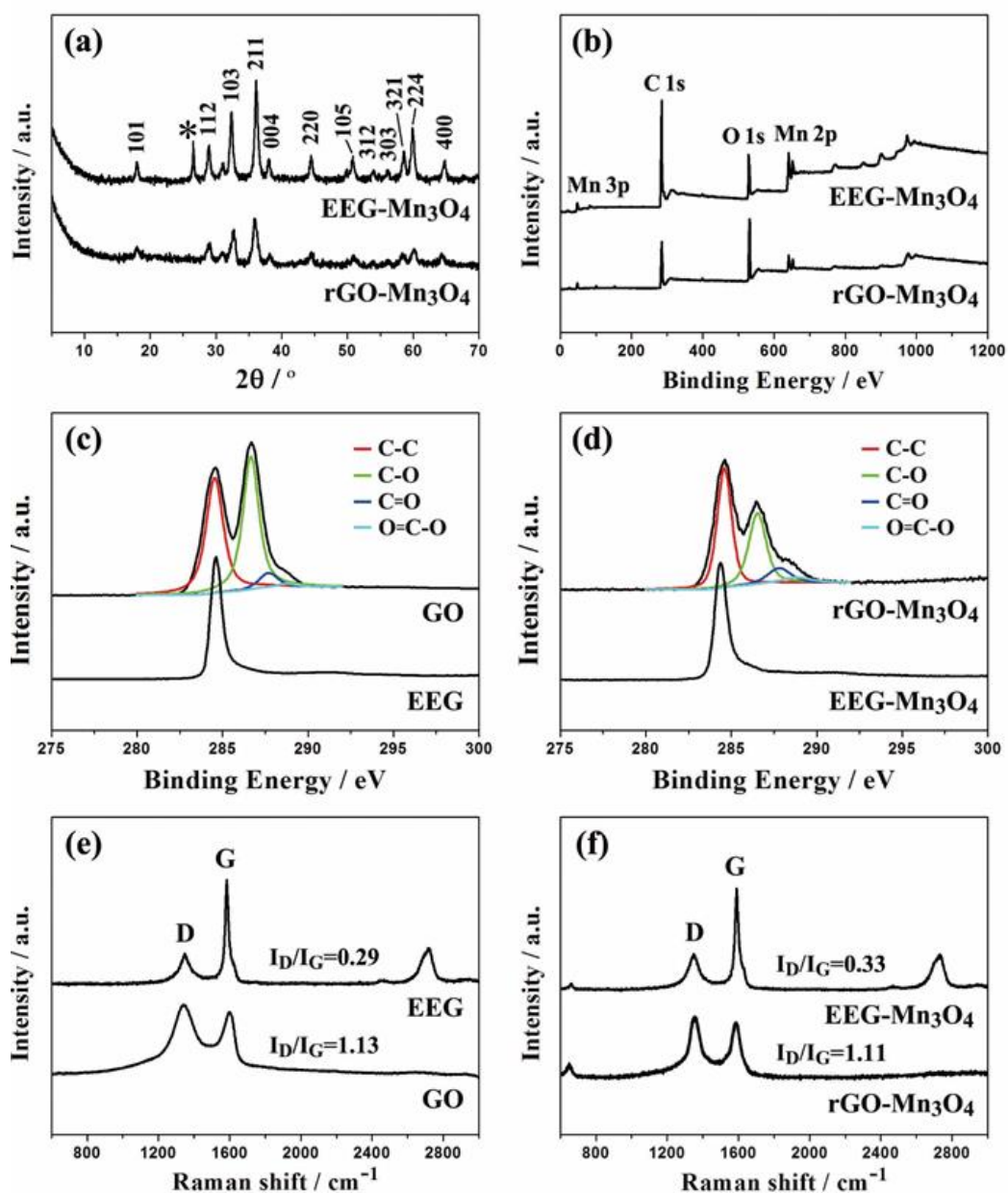
14

Fig. 4 (a) XRD patterns and (b) XPS survey spectra of rGO-Mn_3O_4 and EEG-Mn_3O_4. High-resolution C1s XPS (c, d) and Raman (e, f) spectra of GO, EEG, rGO-Mn_3O_4 and EEG-Mn_3O_4.

To further remove O-containing groups in rGO in order to increase its conductivity, rGO-Mn_3O_4 was hydrothermally treated at 160 °C (designated HrGO-Mn_3O_4). The size and morphology of the Mn_3O_4 nanocrystals did not change (**Fig. S5a**), but their

15

crystallinity increased as the XRD peaks became sharper (**Fig. S5b**). The peaks related to O-containing groups almost disappear in the C 1s XPS spectrum (**Fig. S5c**), showing that most O-containing groups in rGO have been removed. Raman spectrum of HrGO-Mn_3O_4 (**Fig. S5d**) shows a similar I_D/I_G value (1.10) to that of rGO-Mn_3O_4 (1.11), indicating again that the structural defects cannot be repaired by removing the O-containing groups. As it can be expected, EEG with few defects leads to a relatively high conductivity of EEG-Mn_3O_4 (24.0 S cm^{-1}) in comparison with rGO-Mn_3O_4 (6.1 S cm^{-1}) and HrGO-Mn_3O_4 (14.5 S cm^{-1}) (**Table 1**).

3.2 Electrochemical performance

The electrochemical performance of EEG-Mn_3O_4 was firstly studied by cyclic voltammetry. The CV curve (**Fig. 5a**) shows three reduction peaks between ~0.8 and ~1.7 V in the first scan, which is assigned to the formation of solid-electrolyte interface (SEI) films and a concomitant initial reduction of Mn_3O_4 to MnO. Another sharp peak at ~0.08 V corresponds to the reduction of MnO to metallic Mn, which is consistent with the reports for Mn_3O_4-based electrodes [33,34]. The peaks in the reverse sweep are from the oxidation of metallic Mn to the oxide. In the subsequent cycles, the reduction peaks shift to ~0.2 and ~0.9 V due to the polarization of the electrode. Moreover, the 6th cycle almost overlaps with the 3rd cycle, indicating a good electrochemical reversibility of EEG-Mn_3O_4.

The electrochemical performance of rGO-Mn_3O_4, HrGO-Mn_3O_4 and EEG-Mn_3O_4 was subsequently evaluated by galvanostatic measurements. As shown in **Fig. 5b**, the initial capacities of EEG-Mn_3O_4, HrGO-Mn_3O_4 and rGO-Mn_3O_4 are ~1438, ~1277 and 1168 mA h g^{-1} at 0.1 C respectively, higher than the theoretical capacity of Mn_3O_4

($\sim$936 mA h g^{-1}). The excess capacities could be attributed to the formation of SEI film on the surface of the composite, which is commonly observed for other graphene-based metal oxides [5,6]. Besides, the formed SEI film also results in large irreversible capacity losses and poor coulombic efficiencies in the initial cycles. Coating graphene hybrids with ultrathin TiO$_2$ nanofilms could effectively reduce their irreversible capacities and improve their initial coulombic efficiencies [35,36]. The capacities of rGO-Mn$_3$O$_4$ and HrGO-Mn$_3$O$_4$ decreases dramatically in the initial cycles and do not change much after 100 cycles. HrGO-Mn$_3$O$_4$ shows a higher capacity than rGO-Mn$_3$O$_4$ after 200 cycles ($\sim$596 mA h g^{-1} vs. $\sim$349 mA h g^{-1}) because the GO substrate in HrGO-Mn$_3$O$_4$ is highly reduced. As expected, EEG-Mn$_3$O$_4$ exhibits the best cycle and rate performance among these graphene hybrids. The capacity of EEG-Mn$_3$O$_4$ maintains at $\sim$914 mA h g^{-1} after 200 cycles at 0.1 C, which is comparable to the theoretical capacity of Mn$_3$O$_4$ ($\sim$936 mA h g^{-1}). The cycling stability of EEG-Mn$_3$O$_4$ is also impressive in the light of a capacity retention of 97% versus the second cycle ($\sim$944 mA h g^{-1}). When the current density increases to 2 C (**Fig. 5c**), EEG-Mn$_3$O$_4$ exhibits a remarkable capacity of $\sim$497 mA h g^{-1} after 30 cycles, much higher than those of rGO-Mn$_3$O$_4$ ($\sim$135 mA h g^{-1}) and HrGO-Mn$_3$O$_4$ ($\sim$315 mA h g^{-1}). EEG-Mn$_3$O$_4$ ($\sim$30 wt% loading) also exhibits better electrochemical performance than HrGO-Mn$_3$O$_4$ obtained by hydrothermal treatment of rGO-Mn$_3$O$_4$ ($\sim$30 wt% loading) (**Fig. S6**), indicating that EEG is a better carbon substrate than rGO or HrGO no matter when the oxide loading is low or high.

Higher loadings of Mn$_3$O$_4$ on EEG and HrGO were also prepared (**Fig. S7**). Compared to EEG-Mn$_3$O$_4$ ($\sim$60 wt%), EEG-Mn$_3$O$_4$ ($\sim$75 wt%) shows slightly worse

17

electrochemical performance due to the aggregation of Mn_3O_4 nanocrystals and increased resistance at high loading.
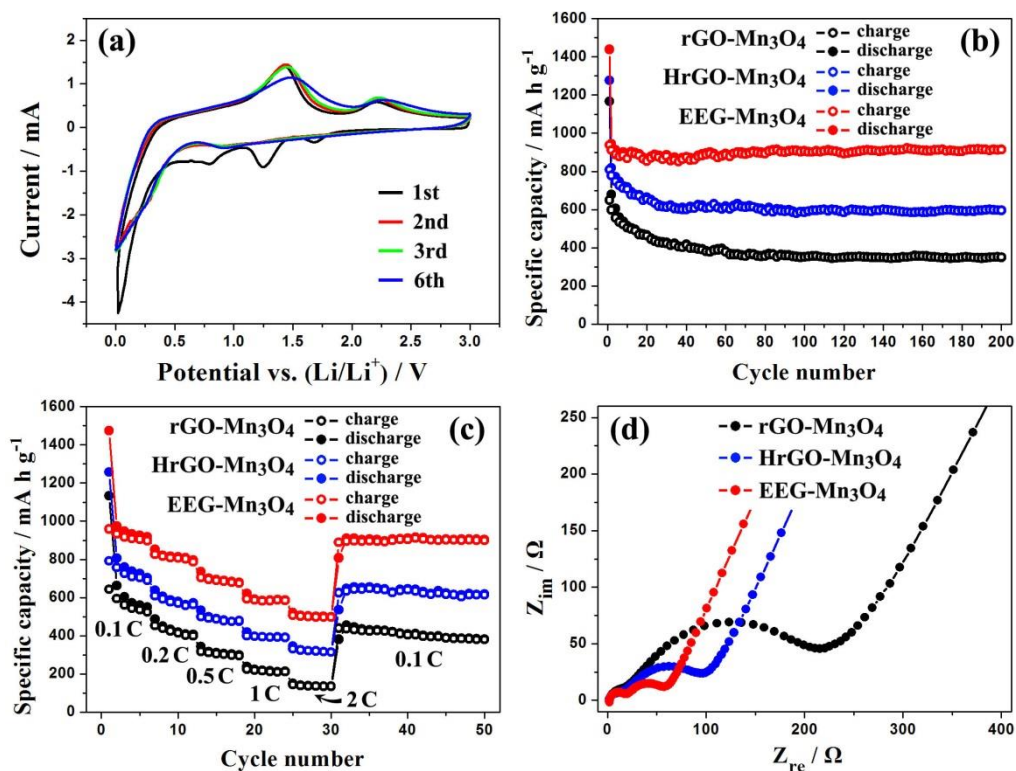

Fig. 5 (a) CV curve of EEG-Mn_3O_4 at a scan rate of 0.5 mV s^{-1}. (b) Cycle performance at 0.1 C, (c) rate performances at 0.1–2 C and (d) electrochemical impedance spectra after 3 cycles of rGO-Mn_3O_4, HrGO-Mn_3O_4 and EEG-Mn_3O_4.

The high electrical conductivity of EEG-Mn_3O_4 is further confirmed by electrochemical impedance spectroscopy (EIS) measurements. Nyquist plots (**Fig. 5d**) show two overlapping semicircles in the high and medium frequency ranges, corresponding to the SEI film resistance (R_f) and the charge transfer resistance (R_{ct}), respectively [37,38]. The R_f and R_{ct} values of the samples were simulated via a Randles equivalent circuit model (**Fig. S8**, **Table 1**). Apparently, EEG-Mn_3O_4 has remarkably

lower R_f (17.0 Ω) and R_{ct} (32.6 Ω) than rGO-Mn$_3$O$_4$ (24.7 and 143.3 Ω) and HrGO-Mn$_3$O$_4$ (17.2 and 61.8 Ω), confirming the fast electron transfer in EEG-Mn$_3$O$_4$.

The stability of the composites after 100 cycles was verified by TEM. As seen in **Fig. S9**, Mn$_3$O$_4$ nanocrystals aggregate on the HrGO substrate, whereas the nanocrystals are still well separated on EEG. The superior structural stability of EEG-Mn$_3$O$_4$ can be attributed to the excellent mechanical properties of EEG [39,40], which effectively withstand the stress caused by the volume change of Mn$_3$O$_4$.

3.3 Growth mechanism of Mn$_3$O$_4$ on EEG

To explore the nucleation and growth mechanism of Mn$_3$O$_4$ nanocrystals on EEG, some comparative experiments were carried out. The Mn-containing molecules in DMF with and without addition of water were identified by mass spectroscopy. It is indicated that water addition facilitates the hydrolysis of Mn(acac)$_2$ to form larger polymerized molecules (**Fig. S10a**), e.g. dimer $[HMn_2O(H_2O)_6(acac)_2]^+$, trimer $[HMn_3O_2(H_2O)_{10}(acac)_2]^+$, tetramer $[HMn_4O_3(H_2O)_{14}(acac)_2]^+$, and pentamer $[HMn_5O_4(H_2O)_{18}(acac)_2]^+$, etc (**Fig. S11**). We anticipate that these polymer molecules can be adsorbed on the surface of EEG via multiple connecting sites, and then aggregate into larger clusters due to strong inter-molecular interactions.

The adsorption of molecules on an inert surface is actually a balance of adsorption and desorption. When a small molecule is adsorbed on the surface via a single interaction site, its life time on the surface would be very short. In other words, the molecule may leave the surface before forming a larger cluster with other molecules. For a polymer molecule with multiple interaction sites, when dissociation takes place at some sites, the linkage at other sites can still hold the polymer molecule on the surface,

19

making it easier to form a cluster. Therefore polymer precursor molecules may overcome the inert property of the EEG surface, allowing surface adsorption, formation of clusters, nucleation in the clusters and finally, forming crystallites.

Indeed, polymer like particles were often observed from TEM images of EEG nanosheets (**Fig. S12**) collected from this sample before the water bath treatment. These loose and irregular particles were basically amorphous, as the SAED pattern shows no diffraction rings corresponding to Mn_3O_4 crystals. The XRD pattern shows only a strong peak corresponding to the stacking of graphene nanosheets (**Fig. 6b**). On the other hand, existence of Mn in the polymer (**Fig. 6a**) indicates that the deposited particles are likely polymerized $Mn(acac)_2$. The low ratio of Mn : C detected from EDX indicates a lower density of Mn than that in the specimen after forming Mn_3O_4 nanocrystals. **Fig. 6c** is a HRTEM image of such an EEG nanosheet. The area marked by A has a thin layer of the polymer and the area marked B is a thick layer of the polymer. The area marked by C is EEG with deposition of very few molecules. The image also shows that crystallization of the polymer particles occurs already, an example area with partial crystallization being indicated by an arrow.

After the water bath treatment, the polymer particles gradually decomposed and Mn_3O_4 nanocrystals firmly deposit on the EEG surface (**Fig. 1**). The process of aggregation of precursor molecules, followed by nucleation and crystal growth in the aggregates was often observed in the so-called reversed crystal growth mechanism [41,42].
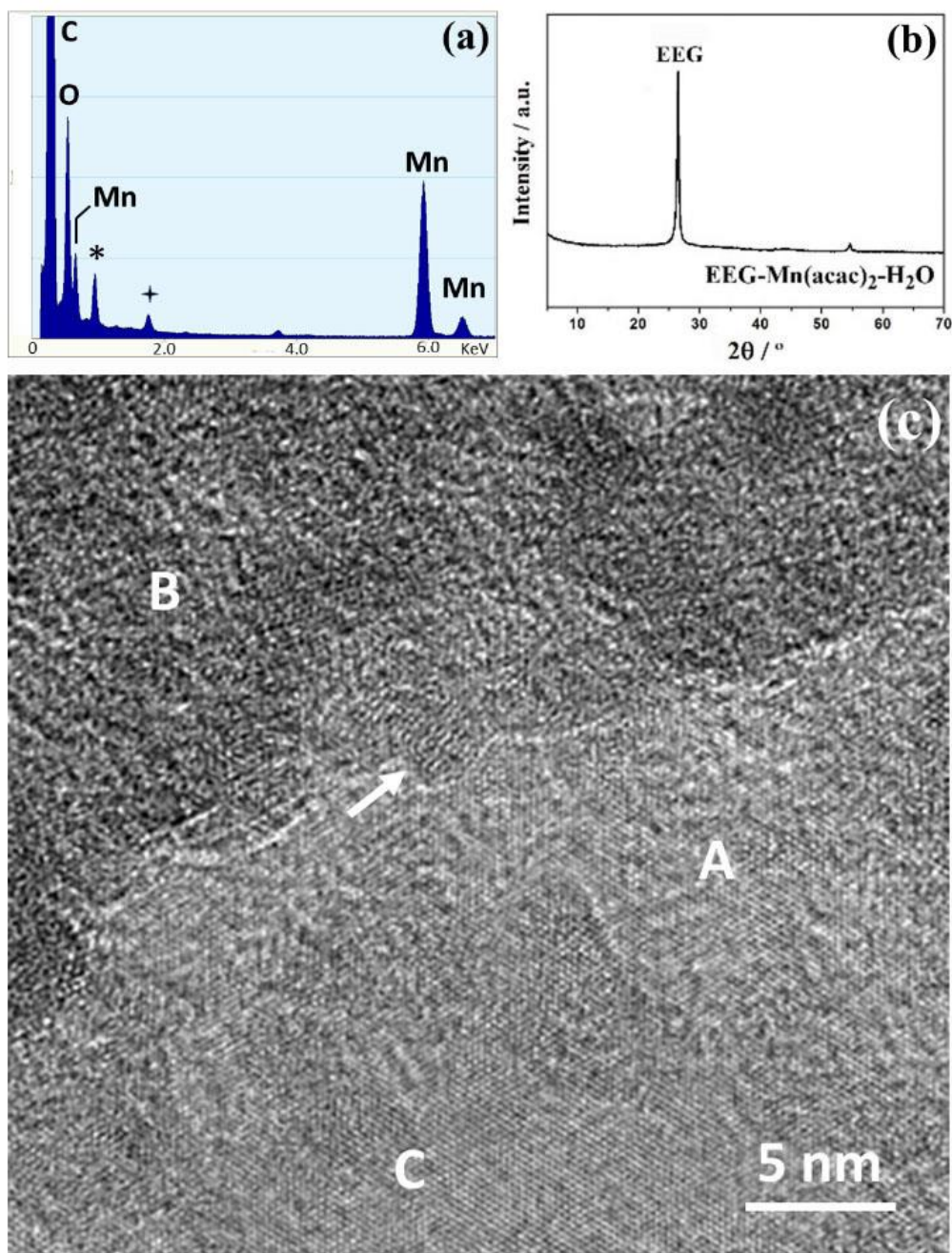
Fig. 6 (a) EDX spectrum, (b) XRD pattern and (c) HRTEM image of an EEG nanosheet collected from a suspension of DMF with addition of Mn(acac)$_2$ and H$_2$O.

On the contrary, polymerization did not happen in the DMF suspension of EEG and Mn(acac)$_2$ without addition of water and only one peak of Mn(acac)$_2$ was observed from the mass spectrum (**Fig. S10b**). SEM images of the EEG nanosheets collected

from the synthetic suspension of DMF with $Mn(acac)_2$, but without addition of water, designated EEG-$Mn(acac)_2$, show scarcely any polymers on the EEG surface. A typical example is shown in **Fig. S13a**. On the other hand, many particles can be seen on the EEG nanosheets collected from the suspension with water, designated EEG-$Mn(acac)_2$-H_2O, as shown in **Fig. S13b**. In addition, Mn element was not detected in EDX spectrum of EEG-$Mn(acac)_2$. After water bath treatment, the surface of EEG nanosheets from the suspension without water addition is also clean (**Fig. S13c**) without Mn peak detected by EDX, while many Mn_3O_4 nanocrystals were observed on the EEG surface of EEG-$Mn(acac)_2$-H_2O (**Fig. S13d**). Consequently, the water enhanced formation of large polymer clusters in DMF is essential to the growth of Mn_3O_4 nanocrystals on EEG.

The effects of the amount of water and the temperature of water bath on the growth of M_3O_4 nanocrystals on EEG were also studied. EEG-Mn_3O_4 prepared by decreasing the amount of water to 0.5 mL and the temperature of water bath to 40 °C are denoted as EEG-Mn_3O_4-SW and EEG-Mn_3O_4-LT, respectively. SEM images of EEG-Mn_3O_4-SW and EEG-Mn_3O_4-LT (**Fig. S14a,b**) show that small numbers of Mn_3O_4 nanoparticles are formed on the surface of EEG. Furthermore, the XRD peaks corresponding to the structure of Mn_3O_4 are very weak (**Fig. S14c**), implying that these samples contain low loading and low crystallinity of Mn_3O_4. TGA curves (**Fig. S14d**) indicate that the contents of Mn_3O_4 in EEG-Mn_3O_4-SW and EEG-Mn_3O_4-LT are only 25.8 and 17.7 wt%, respectively, much lower than that in EEG-Mn_3O_4 (58.6 wt%). Accordingly, the factors that affect the hydrolysis and condensation of $Mn(acac)_2$ in DMF such as added water and heating temperature play important roles in the growth of Mn_3O_4 nanocrystals on EEG.

Consequently, the growth of Mn_3O_4 nanocrystals on EEG in the present work does not follow the classical route, i.e. nucleation on the EEG surface followed by layer-by-layer deposition of the building units. The newly observed crystal growth includes three steps as shown in **Scheme 1**. Step (i), $Mn(acac)_2$ molecules are hydrolyzed with an assistance of a small amount of water in DMF, and then polymerized into large molecules. Step (ii), the polymer molecules further aggregate into large clusters with a strong inter-molecular interaction and are adsorbed on the EEG surface via multiple interaction sites. Step (iii), during the water bath treatment, the polymer molecules undergo further hydrolysis, dehydration, leading to the formation of Mn_3O_4 nanocrystals on the EEG surface.
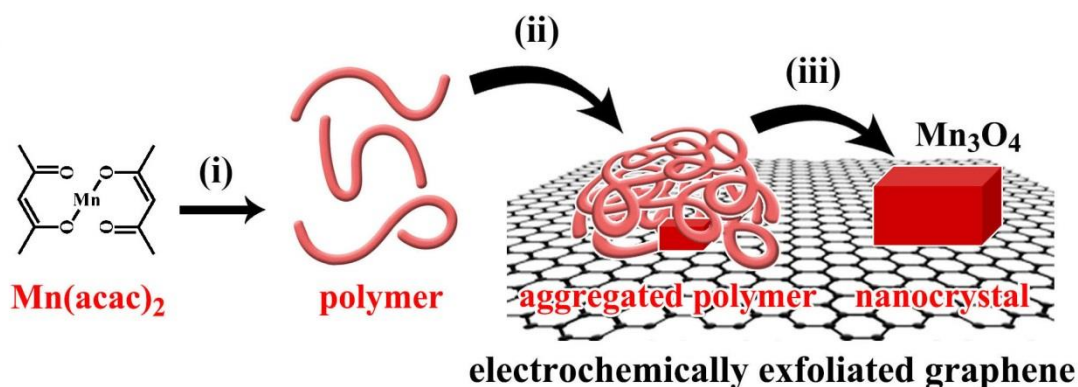
Scheme 1 Schematic illustration of the growth mechanism of Mn_3O_4 nanocrystals on the EEG surface.

To prove the universality of this method, other Mn-containing precursors such as manganese acetate was used to prepare Mn_3O_4 nanoparticles on the surface of EEG. XRD pattern and SEM image (**Fig. S15**) indicate that Mn_3O_4 nanoparticles successfully form on the surface of EEG. This kind of EEG-Mn_3O_4 was prepared under solvothermal

conditions rather than in water bath, implying that the anions have an impact on the growth of Mn_3O_4 nanocrystals on EEG.

4. Conclusions

In summary, a facile method for the preparation of EEG-Mn_3O_4 under gentle conditions has been developed. The long standing difficulty of growing metal oxide nanocrystals on intrinsic graphene due to the inert nature of the graphene surface has been overcome by deposition of polymerized precursor. The produced composites show much better electrochemical properties than the composites using rGO. The new method is environmentally friendly because the pre-treatment of graphene can be avoided and the temperature of crystal growth can be reduced. The method can be used for crystal growth of many other metal oxides on intrinsic graphene surface, in order to make new energy materials for a wide range of applications.

Acknowledgements

References

[1] K. S. Novoselov, A. K. Geim, S. V. Morozov, D. Jiang, Y. Zhang, S. V. Dubonos, I. V. Grigorieva, A. A. Firsov, Electric field effect in atomically thin carbon films, Science 306 (2004) 666–669. https://doi.org/10.1126/science.1102896.

[2] A. K. Geim, K. S. Novoselov, The rise of graphene, Nat. Mater. 6 (2007) 183–191. https://doi.org/10.1038/nmat1849.

[3] Z. G. Zhang, J. P. Zhao, J. Zhou, Y. Zhao, X. N. Tang, S. P. Zhuo, Interfacial engineering of metal oxide/graphene nanoscrolls with remarkable performance for lithium ion batteries, Energy Storage Mater. 8 (2017) 35–41. https://doi.org/10.1016/j.ensm.2017.03.003.

[4] X. T. Guo, S. S. Zheng, G. X. Zhang, X. Xiao, X. R. Li, Y. X. Xu, H. G. Xue, H. Pang, Nanostructured graphene-based materials for flexible energy storage, Energy Storage Mater. 9 (2017) 150–169. https://doi.org/10.1016/j.ensm.2017.07.006.

[5] S. Yang, W. B. Yue, J. Zhu, Y. Ren, X. J. Yang, Graphene-based mesoporous SnO_2 with enhanced electrochemical performance for lithium-ion batteries, Adv. Funct. Mater. 23 (2013) 3570–3576. https://doi.org/10.1002/adfm.201203286.

[6] H. L. Wang, L. –F. Cui, Y. Yang, H. S. Casalongue, J. T. Robinson, Y. Y. Liang, Y. Cui, H. J. Dai, Mn_3O_4-graphene hybrid as a high-capacity anode material for lithium ion batteries, J. Am. Chem. Soc. 132 (2010) 13978–13980. https://doi.org/10.1021/ja105296a.

[7] H. Jiang, L. P. Yang, C. Z. Li, C. Y. Yan, P. S. Lee, J. Ma, High-rate electrochemical capacitors from highly graphitic carbon–tipped manganese oxide/mesoporous carbon/manganese oxide hybrid nanowires, Energy Environ. Sci. 4 (2011) 1813–1819. https://doi.org/10.1039/C1EE01032H.

[8] S. K. Bikkarolla, F. J. Yu, W. Z. Zhou, P. Joseph, P. Cumpson, P. Papakonstantinou, A three-dimensional Mn_3O_4 network supported on a nitrogenated graphene

electrocatalyst for efficient oxygen reduction reaction in alkaline media, J. Mater. Chem. A 2 (2014) 14493−14501. https://doi.org/10.1039/C4TA02279C.

[9] Z. Y. Cai, L. Xu, M. Y. Yan, C. H. Han, L. He, K. M. Hercule, C. J. Niu, Z. F. Yuan, W. W. Xu, L. B. Qu, K. N. Zhao, L. Q. Mai, Manganese oxide/carbon yolk−shell nanorod anodes for high capacity lithium batteries, Nano Lett. 15 (2015) 738−744. https://doi.org/10.1021/nl504427d.

[10] Y. T. Hu, C. Guan, G. X. Feng, Q. Q. Ke, X. L. Huang, J. Wang, Flexible asymmetric supercapacitor based on structure-optimized Mn_3O_4/reduced graphene oxide nanohybrid paper with high energy and power density, Adv. Funct. Mater. 25 (2015) 7291−7299. https://doi.org/10.1002/adfm.201503528.

[11] J. Park, Y. S. Cho, S. J. Sung, M. Byeon, S. J. Yang, C. R. Park, Characteristics tuning of graphene-oxide-based-graphene to various end-uses, Energy Storage Mater. 14 (2018) 8−21. https://doi.org/10.1016/j.ensm.2018.02.013.

[12] H. Turgut, Z. R. Tian, F. J. Yu, W. Z. Zhou, Multivalent cation cross-linking suppresses highly energetic graphene oxide's flammability, J. Phys. Chem. C 121 (2017) 5829−5835. https://doi.org/10.1021/acs.jpcc.6b13043.

[13] S. Yang, S. Brüller, Z. S. Wu, Z. Y. Liu, K. Parvez, R. H. Dong, F. Richard, P. Samorì, X. L. Feng, K. Müllen, Organic radical-assisted electrochemical exfoliation for the scalable production of high-quality graphene, J. Am. Chem. Soc. 137 (2015) 13927−13932. https://doi.org/10.1021/jacs.5b09000.

[14] S. Yang, M. R. Lohe, K. Müllen, X. L. Feng, New-generation graphene from electrochemical approaches: production and applications, Adv. Mater. 28 (2016) 6213–6221. https://doi.org/10.1002/adma.201505326.

[15] N. G. Shang, P. Papakonstantinou, S. Sharma, G. Lubarsky, M. Li, D. W. McNeill, A. J. Quinn, W. Z. Zhou, R. Blackley, Controllable selective exfoliation of high-quality graphene nanosheets and nanodots by ionic liquid assisted grinding, Chem. Commun. 48 (2012) 1877–1879. https://doi.org/10.1039/C2CC17185F.

[16] H. L. Wang, H. S. Casalongue, Y. Y. Liang, H. J. Dai, $Ni(OH)_2$ nanoplates grown on graphene as advanced electrochemical pseudocapacitor materials, J. Am. Chem. Soc. 132 (2010) 7472–7477.https://doi.org/10.1021/ja102267j.

[17] G. M. Zhou, D. -W. Wang, L. -C. Yin, N. Li, F. Li, H. –M. Cheng, Oxygen bridges between NiO nanosheets and graphene for improvement of lithium storage, ACS Nano 6 (2012) 3214–3223. https://doi.org/10.1021/nn300098m.

[18] W. Y. Zhang, Y. Zeng, N. Xiao, H. H. Hng, Q. Y. Yan, One-step electrochemical preparation of graphene-based heterostructures for Li storage, J. Mater. Chem. 22 (2012) 8455–8461. https://doi.org/10.1039/C2JM16315B.

[19] B. Zhao, L. Jiang, X. L. Zeng, K. Zhang, M. M. F. Yuen, J. B. Xu, X. Z. Fu, R. Sun, C. P. Wong, A highly thermally conductive electrode for lithium ion batteries, J. Mater. Chem. A 4 (2016) 14595–14604. https://doi.org/10.1039/C6TA04774B.

[20] Z. Y. Xia, D. Wei, E. Anitowska, V. Bellani, L. Ortolani, V. Morandi, M. Gazzano, A. Zanelli, S. Borini, V. Palermo, Electrochemically exfoliated graphene oxide/iron oxide composite foams for lithium storage, produced by simultaneous graphene

reduction and Fe(OH)$_3$ condensation, Carbon 84 (2015) 254–262. https://doi.org/10.1016/j.carbon.2014.12.007.

[21] Y. Hou, M. R. Lohe, J. Zhang, S. H. Liu, X. D. Zhuang, X. L. Feng, Vertically oriented cobalt selenide/NiFe layered-double-hydroxide nanosheets supported on exfoliated graphene foil: an efficient 3D electrode for overall water splitting, Energy Environ. Sci. 9 (2016) 478–483. https://doi.org/10.1039/C5EE03440J.

[22] W. Wei, G. Wang, S. Yang, X. L. Feng, K. Müllen, Efficient coupling of nanoparticles to electrochemically exfoliated graphene, J. Am. Chem. Soc. 137 (2015) 5576−5581. https://doi.org/10.1021/jacs.5b02284.

[23] W. S. Hummers, R. E. Offeman, Preparation of graphitic oxide, J. Am. Chem. Soc. 80 (1958) 1339–1339. https://doi.org/10.1021/ja01539a017.

[24] Q. S. Huang, G. Wang, L. W. Guo, Y. P. Jia, J. J. Lin, K. Li, W. J. Wang, X. L. Chen, Approaching the intrinsic electron field-emission of a graphene film consisting of quasi-freestanding graphene strips, Small 7 (2011) 450–454. https://doi.org/10.1002/smll.201001502.

[25] J. H. Warner, M. H. Rümmeli, L. Ge, T. Gemming, B. Montanari, N. M. Harrison, B. Büchner, G. A. D. Briggs, Structural transformations in graphene studied with high spatial and temporal resolution, Nat. Nanotechnol. 4 (2009) 500–504. https://doi.org/10.1038/nnano.2009.194.

[26] L. Li, G. M. Zhou, Z. Weng, X. -Y. Shan, F. Li , H. -M. Cheng, Monolithic Fe$_2$O$_3$/graphene hybrid for highly efficient lithium storage and arsenic removal, Carbon 67 (2014) 500–507. https://doi.org/10.1016/j.carbon.2013.10.022.

[27] Z. J. Li, D. B. Kong, G. M. Zhou, S. D. Wu, W. Lv, C. Luo, J. -J. Shao, B. H. Li, F. Y. Kang, Q. -H. Yang, Twin-functional graphene oxide: compacting with Fe_2O_3 into a highvolumetric capacity anode for lithium ion battery, Energy Storage Mater. 6 (2017) 98–103. https://doi.org/10.1016/j.ensm.2016.09.005.

[28] G. M. Zhou, L. Li, Q. Zhang, N. Li, F. Li, Octahedral Co_3O_4 particles threaded by carbon nanotube arrays as integrated structure anodes for lithium ion batteries, Phys. Chem. Chem. Phys. 15 (2013) 5582–5587. https://doi.org/10.1039/c3cp50221j.

[29] K. Chen, F. Zhang, J. Y. Sun, Z. Z. Li, L. Zhang, A. Bachmatiuk, Z. Y. Zou, Z. L. Chen, L. Y. Zhang, M. H. Rümmeli, Z. F. Liu, Growth of defect-engineered graphene on manganese oxides for Li-ion storage, Energy Storage Mater. 12 (2018) 110–118. https://doi.org/10.1016/j.ensm.2017.12.001.

[30] P. Zhao, W. B. Yue, X. Yuan, H. Y. Bao, Exceptional lithium anodic performance of Pd-doped graphene-based SnO_2 nanocomposite, Electrochim. Acta 225 (2017) 322–329. https://doi.org/10.1016/j.electacta.2016.12.124.

[31] L. Shang, T. Bian, B. H. Zhang, D. H. Zhang, L. -Z. Wu, C. -H. Tung, Y. D. Yin, T. R. Zhang, Graphene-supported ultrafine metal nanoparticles encapsulated by mesoporous silica: robust catalysts for oxidation and reduction reactions, Angew. Chem. Int. Ed. 53 (2014) 250–254. https://doi.org/10.1002/anie.201306863.

[32] L. Z. Sheng, S. C. Liang, T. Wei, J. Chang, Z. M. Jiang, L. H. Zhang, Q. H. Zhou, J. L. Zhou, L. L. Jiang, Z. J. Fan, Space-confinement of MnO nanosheets in densely stacked graphene: Ultra-high volumetric capacity and rate performance for lithium-ion batteries, Energy Storage Mater. 12 (2018) 94−102. https://doi.org/10.1016/j.ensm.2017.11.014.

[33] J. -G. Wang, D. D. Jin, R. Zhou, X. Li, X. -R Liu, C. Shen, K. Y. Xie, B. H. Li, F. Y. Kang, B. Q. Wei, Highly flexible graphene/Mn_3O_4 nanocomposite membrane as advanced anodes for Li-ion batteries, ACS Nano, 10 (2016) 6227−6234. https://doi.org/10.1021/acsnano.6b02319.

[34] R. Lin, W. B. Yue, F. Z. Niu, J. Ma, Novel strategy for the preparation of graphene-encapsulated mesoporous metal oxides with enhanced lithium storage, Electrochim. Acta 205 (2016) 85–94. https://doi.org/10.1016/j.electacta.2016.04.095.

[35] F. -F. Cao, Y. -G. Guo, S. -F. Zheng, X. -L. Wu, L. -Y. Jiang, R. -R. Bi, L. -J. Wan, J. Maier, Symbiotic coaxial nanocables: facile synthesis and an efficient and elegant morphological solution to the lithium storage problem, Chem. Mater. 22 (2010) 1908–1914. https://doi.org/10.1021/cm9036742.

[36] S. T. Liu, W. B. Yue, C. Zhang, D. J. Du, X. J. Yang, Enhanced lithium storage properties of graphene-based metal oxides by coating with amorphous TiO_2 nanofilms, J. Alloys Compd. 769 (2018) 293–300. https://doi.org/10.1016/j.jallcom.2018.08.014.

[37] S. S. Tao, W. B. Yue, M. Y. Zhong, Z. J. Chen, Y. Ren, Fabrication of Graphene-Encapsulated porous carbon–metal oxide composites as anode materials for lithium-ion batteries, ACS Appl. Mater. Interfaces 6 (2014) 6332−6339. https://doi.org/10.1021/am501551h.

[38] L. Zhao, M. M. Gao, W. B. Yue, Y. Jiang, Y. Wang, Y. Ren, F. Q. Hu, Sandwich-structured graphene-Fe_3O_4@carbon nanocomposites for high-performance lithium-ion batteries, ACS Appl. Mater. Interfaces 7 (2015) 9709−9715. https://doi.org/10.1021/acsami.5b01503.

[39] K. Parvez, Z. -S. Wu, R. J. Li, X. J. Liu, R. Graf, X. L. Feng, K. Müllen, Exfoliation of graphite into graphene in aqueous solutions of inorganic salts, J. Am. Chem. Soc. 136 (2014) 6083–6091. https://doi.org/10.1021/ja5017156.

[40] G. Wang, J. Zhang, S. Yang, F. X. Wang, X. D. Zhuang, K. Müllen, X. L. Feng, Vertically aligned MoS_2 nanosheets patterned on electrochemically exfoliated graphene for high-performance lithium and sodium storage, Adv. Energy Mater. 8 (2018) 1702254. https://doi.org/10.1002/aenm.201702254.

[41] J. F. Yao, D. Li, X. Y. Zhang, C. H. Kong, W. B. Yue, W. Z. Zhou, H. T. Wang, Cubes of zeolite A with an amorphous core, Angew. Chem. Int. Ed. 47 (2008) 8397–8399. https://doi.org/10.1002/anie.200802823.

[42] W. Z. Zhou, Reversed crystal growth: implications for crystal engineering, Adv. Mater. 22 (2010) 3086–3092. https://doi.org/10.1002/adma.200904320.